







**Cavity-QED simulation of a quantum metamaterial with tunable disorder**

Grigoriy S. Mazhorin <sup>1,2,3</sup> Ilya N. Moskalenko <sup>2,3</sup> Ilya S. Besedin <sup>2,3</sup> Dmitriy S. Shapiro,<sup>4,5,6,\*</sup>  
Sergey V. Remizov,<sup>4,5,7</sup> Walter V. Pogosov <sup>4,8,9</sup> Dmitry O. Moskalev,<sup>4,10</sup> Anastasia A. Pishchimova,<sup>4,10</sup>  
Alina A. Dobronosova,<sup>4,10</sup> I. A. Rodionov <sup>4,10</sup> and Alexey V. Ustinov <sup>2,3,11</sup>

<sup>1</sup>*Moscow Institute of Physics and Technology, Dolgoprudny, 141701, Russia*

<sup>2</sup>*National University of Science and Technology MISiS, 119049 Moscow, Russia*

<sup>3</sup>*Russian Quantum Center, Skolkovo, 143025 Moscow Region, Russia*

<sup>4</sup>*Dukhov Research Institute of Automatics (VNIIA), Moscow 127055, Russia*

<sup>5</sup>*V. A. Kotel'nikov Institute of Radio Engineering and Electronics, Russian Academy of Sciences, Moscow 125009, Russia*

<sup>6</sup>*Institute for Quantum Materials and Technologies, Karlsruhe Institute of Technology, 76021 Karlsruhe, Germany*

<sup>7</sup>*Department of Physics, National Research University Higher School of Economics, Moscow 101000, Russia*

<sup>8</sup>*Institute for Theoretical and Applied Electrodynamics, Russian Academy of Sciences, 125412 Moscow, Russia*

<sup>9</sup>*HSE University, 109028 Moscow, Russia*

<sup>10</sup>*FMN Laboratory, Bauman Moscow State Technical University, Moscow 105005, Russia*

<sup>11</sup>*Physikalisches Institut, Karlsruhe Institute of Technology, 76131 Karlsruhe, Germany*



(Received 3 July 2021; revised 3 November 2021; accepted 16 February 2022; published 23 March 2022)

We explore experimentally a quantum metamaterial based on a superconducting chip with 25 frequency-tunable transmon qubits coupled to a common coplanar resonator. The collective bright and dark modes are probed via the microwave response, i.e., by measuring the transmission amplitude of an external microwave signal. All qubits have individual control and readout lines. Their frequency tunability allows the number  $N$  of resonantly coupled qubits to change and a disorder in their excitation frequencies to be introduced with preassigned distributions. While increasing  $N$ , we demonstrate the expected  $N^{1/2}$  scaling law for the energy gap (Rabi splitting) between bright modes around the cavity frequency. By introducing a controllable disorder and averaging the transmission amplitude over a large number of realizations, we demonstrate a decay of mesoscopic fluctuations which mimics an approach towards the thermodynamic limit. The collective bright states survive in the presence of disorder when the strength of individual qubit coupling to the cavity dominates over the disorder strength.

DOI: [10.1103/PhysRevA.105.033519](https://doi.org/10.1103/PhysRevA.105.033519)

**I. INTRODUCTION**

Recently, superconducting qubits have shown remarkable progress in realizations of scalable quantum computing devices [1] as well as in fundamental studies of circuit quantum electrodynamics (QED) [2]. Quantum circuits based on superconducting qubits allow for testing fermion models [3], geometric phases [4], weak localization [5], topologically ordered states [6–8], and beyond. Various phenomena related to photonic transport and photon-photon interaction can be observed even for a circuit with a single qubit. They appear when microwave photons are transmitted through a qubit circuit which plays the role of a nonlinear oscillator. Examples include photon blockades [9,10], transfer of thermalized photons and measurement of their bunching [11], probing of transmitted photons statistics [12–14], and multiphoton transitions [15].

Multiqubit circuits find their applications in quantum metamaterials [16], which are examples of artificial quantum matter with tunable properties. The dynamics of such metamaterials is governed by quantum-optical models, such

as Dicke [17–19] or Bose-Hubbard [20–22] models, which capture the physics of coupled photonic modes and qubit degrees of freedom.

The major technical challenge for fabrication of multiqubit metamaterials is in making the energy-level separations  $\hbar\epsilon_j$  of many nonidentical qubits as similar as possible. This is required for observing, e.g., a coherent response of the metamaterial and collective bright modes of the system. It has been argued [16,23,24] but not yet proved that, for nontunable qubits, this problem can be overcome by engineering large enough qubit coupling strength  $g$  to the cavity, similar to the way of overcoming the effects of inhomogeneous broadening in lasers made of natural atoms. Coherent response of a metamaterial can be expected if the spread in  $\epsilon_j$  becomes smaller than  $g$ . The individual qubit frequencies  $\epsilon_j$  can be individually controlled by applying local fields to qubits, which obviously becomes more and more technically difficult when increasing the number of qubits in a metamaterial.

Multiqubit metamaterials represent a mesoscopic limit of naturally occurring ensembles consisting of nominally identical atoms or spins. Here, however, the fluctuations are different for each atom and lead to the resonance line broadening in the presence of fluctuating local fields and interactions between atoms. The homogeneously broadened emission

\*dmitrii.shapiro@kit.edu

(lifetime-limited) line has a Lorentzian profile, while the inhomogeneously broadened emission will have a Gaussian profile. While fluctuations in the thermodynamic limit corresponding to a very large number of emitters are well understood and studied in solid-state and molecular spectroscopy, the mesoscopic limit of a countable (not too large) number of emitters is very difficult to explore with natural atoms or spins. Qubit metamaterials may be suitable to fill this knowledge gap. One of the prominent examples is a spin ensemble coupled to a cavity and described by the Tavis-Cummings model [25]. Here, qubits with individual frequency control can be used to introduce a tunable static or dynamic disorder.

In this work we report on an experimental realization of a multiqubit platform that allows one to simulate disorder effects in quantum metamaterials. We have designed and fabricated a superconducting chip based on an array of 25 transmon [26] qubits coupled to a common coplanar resonator. The excitation frequency of every qubit is individually tunable in the GHz range. Hence arbitrary disorder realizations can be easily implemented and studied in this setting.

Our interest in disordered quantum metamaterials is twofold. On one hand, disorder in the frequency of emitters coupled to a cavity is an important technical issue in devices that rely on coherent operation. In the weak-coupling limit, these effects result in inhomogeneous broadening. Simulators based on superconducting qubits are no exception to this issue. Digital simulation approaches based on Trotterization [27] circumvent the issue by using well-calibrated gates to approximate the evolution of a system under a continuous-time Hamiltonian. However, the tradeoff is that even relatively simple simulations require a large number of Trotterization steps, and the increase in the amount of these steps results in a rapidly decaying simulation fidelity. For analog simulators, the disorder in the qubit frequencies stems from the varying critical currents of the Josephson junctions. Correcting for this frequency using superconducting quantum interference devices (SQUIDS) moves the qubits away from their flux sweet spots, which significantly degrades their coherence properties [28]. Thus, for analog simulation, disorder and control infidelity is the major source of errors in the simulation. For digital simulations, various randomization-based techniques have been developed to enhance the signal [29]. Here we use randomization to investigate emergent dark states in a system of transmon qubits coupled to a common microwave cavity.

On the other hand, our interest in disordered quantum metamaterials is motivated by theoretical studies [30–32] where an intriguing interplay between a coherent collective coupling and disorder was discussed. As shown in these studies, the structure of eigenstates has a strong impact on photon transmission. Photon transport measurements allow one to distinguish between localized or semilocalized regimes which exhibit either exponential or power-law decays of transmission amplitude with  $N$ , respectively. In the semilocalized case, wave functions of dark states are neither localized nor extended [32]. We also mention a recent analysis of transmon-based quantum computing networks [33], which are systems with built-in differences in physical qubit parameters. As shown in [33], physics of disordered spin ensembles, in particular, many-body localization, becomes crucial for an operation of those systems.

## II. THEORETICAL BACKGROUND

We address the low-excitation regime, where the rotating-wave approximation is valid and the Dicke model for  $N$  qubits is reduced to the Tavis-Cummings model. For particular qubit frequencies  $\epsilon_j$ , qubit-cavity couplings  $g_j$ , and the cavity mode with the frequency  $\nu_c$ , the Tavis-Cummings model reads as

$$\hat{H} = \nu_c \hat{a}^\dagger \hat{a} + \sum_{j=1}^N \epsilon_j \hat{\sigma}_j^+ \hat{\sigma}_j^- + \sum_{j=1}^N g_j (\hat{\sigma}_j^+ \hat{a} + \hat{a}^\dagger \hat{\sigma}_j^-). \quad (1)$$

Here  $\hat{a}^\dagger$  and  $\hat{a}$  are the photon creation and annihilation operators, and  $\hat{\sigma}_j^+$  and  $\hat{\sigma}_j^-$  are raising and lowering Pauli operators acting upon the  $j$ th two-level system. In the low-energy limit, this Hamiltonian can be represented as a  $N+1$ -dimensional matrix  $\mathcal{H}_{i,j} = \langle \psi_i | \hat{H} | \psi_j \rangle$  after the projection of  $\hat{H}$  on a single excitation basis,  $\{|\psi_i\rangle\}_{i=1}^{N+1} = \{\hat{a}^\dagger |g.s.\rangle; \hat{\sigma}_1^+ |g.s.\rangle; \dots; \hat{\sigma}_N^+ |g.s.\rangle\}$ .

An analysis of the disordered Tavis-Cummings model is complicated because the bright polariton modes are not decoupled from dark states anymore [18], and the relevant Hilbert space is enlarged. This results in such phenomena in inhomogeneously broadened systems as a competition between superradiance and dephasing [34], and cavity protection effect [35].

The respective Green function matrix that takes into account a dissipation to an environment is  $\mathcal{G}(\omega) = (\omega \mathcal{I} + i\mathcal{D} - \mathcal{H})^{-1}$ . Here,  $\mathcal{I} = \delta_{i,j}$  is the identity matrix in the basis  $\{|\psi_i\rangle\}_{i=1}^{N+1}$ , and the matrix  $\mathcal{D} = \text{diag}[\kappa, \Gamma_1, \dots, \Gamma_N]$  is determined by the loss rate in the resonator,  $\kappa$ , and the relaxation from the excited to the ground state in qubits,  $\Gamma_i$ . It can be written through the Green functions of decoupled resonator and qubits,  $G_{\text{ph}}(\omega) = (\omega + i\kappa - \nu_c)^{-1}$  and  $G_{q,j}(\omega) = (\omega + i\Gamma_j - \epsilon_j)^{-1}$ , respectively, as  $\mathcal{G}(\omega) = \begin{bmatrix} G_{\text{ph}}^{-1}(\omega) & -\mathbf{g}^T \\ -\mathbf{g} & \mathbf{G}_q^{-1}(\omega) \end{bmatrix}^{-1}$ . Here the  $N$ -dimensional matrix  $\mathbf{G}_q(\omega) = \delta_{i,j} G_{q,j}(\omega)$  and the vector  $\mathbf{g} = (g_1; g_2; \dots; g_N)^T$  with all coupling constants is introduced. A photonic propagator  $\mathcal{G}_{\text{ph}}(\omega) \equiv [\mathcal{G}(\omega)]_{1,1}$  is found after an expansion of  $\mathcal{G}$  by the nondiagonal part and resummation of the first diagonal element. The result is

$$\mathcal{G}_{\text{ph}}(\omega) = \frac{1}{G_{\text{ph}}^{-1}(\omega) - \mathbf{g}^T \mathbf{G}_q(\omega) \mathbf{g}}. \quad (2)$$

The self-energy term  $\mathbf{g}^T \mathbf{G}_q(\omega) \mathbf{g} = \sum_{j=1}^N \frac{g_j^2}{\omega + i\Gamma_j - \epsilon_j}$  takes into account the diagonal disorder in  $\epsilon_j$  and nondiagonal disorder in  $g_j$ . This Green function approach is in agreement with earlier work [36] where a solution for a susceptibility has been found from the master equation for a density matrix.

By resolving the equation  $\mathcal{G}_{\text{ph}}^{-1}(\omega) = 0$  with respect to  $\omega$  in the absence of the disorder,  $\epsilon_j = \epsilon$ , one finds that the frequencies of bright collective modes are  $\nu_{\pm} = \frac{1}{2}(\nu_c + \epsilon \pm \sqrt{(\nu_c - \epsilon)^2 + 4|\mathbf{g}|^2})$ . If  $g_i = g$  and the resonant condition holds,  $\epsilon_j = \nu_c$ , then one finds a well-known scaling of the energy gap with  $N$  in the Tavis-Cummings model,  $\nu_+ - \nu_- = 2g\sqrt{N}$ . The initial task in this work is thus to demonstrate this scaling law  $\propto N^{1/2}$ . It becomes possible by means of subsequent increase of qubit number tuned into the resonance with the photon mode.

The main aim of this work is to study an ensemble of qubits with tunable diagonal disorder. We set our goals to demonstrate the effect of self-averaging in transmission amplitudes of disordered ensemble and to observe mesoscopic fluctuations which decrease with  $N$ . As long as the diagonal disorder is fully controllable, we set the resonant condition between the resonator mode and all qubits on the average as  $\nu_c = \langle \epsilon_j \rangle$ . The probability density to find the  $j$ th qubit in a frequency range  $[\epsilon; \epsilon + d\epsilon]$  is simulated by a flat function  $p(\epsilon) = \frac{1}{\Delta} \theta(\Delta/2 - |\epsilon - \nu_c|)$ , which is symmetric near  $\epsilon = \nu_c$  and has a controllable spread  $\Delta$ . The nondiagonal disorder effects are less interesting. In our regime of low excitation numbers it results in a renormalization of the effective coupling. This can be seen from the self-energy term where  $g_i$  appear in numerators. Oppositely,  $\epsilon_j$  appear in denominators and the averaging by this variable becomes more nontrivial.

To explore the mesoscopic effects in the qubit metamaterial, we collect data for the transmission coefficient  $S_{21}$  of the microwave probe signal sent at the cavity bare frequency  $\omega = \nu_c$ . As follows from in-out theory where a matching of reflected and transmitted waves is preformed, the transmission coefficient is related to the Green function (2) as follows:  $S_{21} = \sqrt{\gamma_{in}\gamma_{out}} \mathcal{G}_{ph}(\nu_c)$ . Here  $\gamma_{in}$  and  $\gamma_{out}$  are radiation rates from the resonator into *in*- and *out*-waveguides.

Let us analyze  $\langle S_{21} \rangle$  where the averaging is based on a large number of diagonal disorder realizations with the probability density  $p(\epsilon)$ . We consider first the limit of large  $N$  where, similarly to the thermodynamic limit, fluctuations are suppressed and self-averaging can be applied. Namely, the sum from (2) is replaced by the integral with  $p(\epsilon)$ , which is the density of states analog. One finds  $\mathbf{g}^T \mathbf{G}_q(\omega) \mathbf{g} = \pi g^2 N / \Delta$ , and, consequently, the transmission coefficient is

$$\langle S_{21} \rangle = \sqrt{\gamma_{in}\gamma_{out}} \frac{-i}{\kappa + \pi g^2 N / \Delta}. \quad (3)$$

The detailed derivation is presented in Appendix A. Mesoscopic fluctuations  $\Delta S_{21} \equiv S_{21} - \langle S_{21} \rangle$ , which are considered as a random value corresponding to a particular disorder realization, appear at finite  $N$ . They are found as follows in the leading order by the finite  $N$ :

$$\langle |\Delta S_{21}|^2 \rangle = \gamma_{in}\gamma_{out} \frac{\pi N g^4}{2\Gamma\Delta(\kappa + \pi g^2 N / \Delta)^4}. \quad (4)$$

One sees that the average decays as  $\langle S_{21} \rangle \propto N^{-1}$  while fluctuations as  $\propto N^{-3}$  at large  $N$  limit. In our experiment we use the results (3) and (4) to fit the measured data.

### III. QUANTUM CIRCUIT AND MEASUREMENT SETUP

Here we present first our experimental setting, which involves 25 superconducting transmon qubits. A particular qubit, measurement scheme, and equivalent circuit are shown in Figs. 1(a)–1(d), respectively. Qubits are capacitively coupled to a common cavity realized as a  $\lambda/2$  coplanar waveguide resonator [panel (a), brown color]. The cavity is terminated with the input transmission line (cyan color). A transmon qubit [panel (b)], at one of its ends, involves a short segment running close to the common cavity conductor (brown color). This results in a strong capacitive qubit-cavity coupling. At the other end the transmon is connected to an individual flux

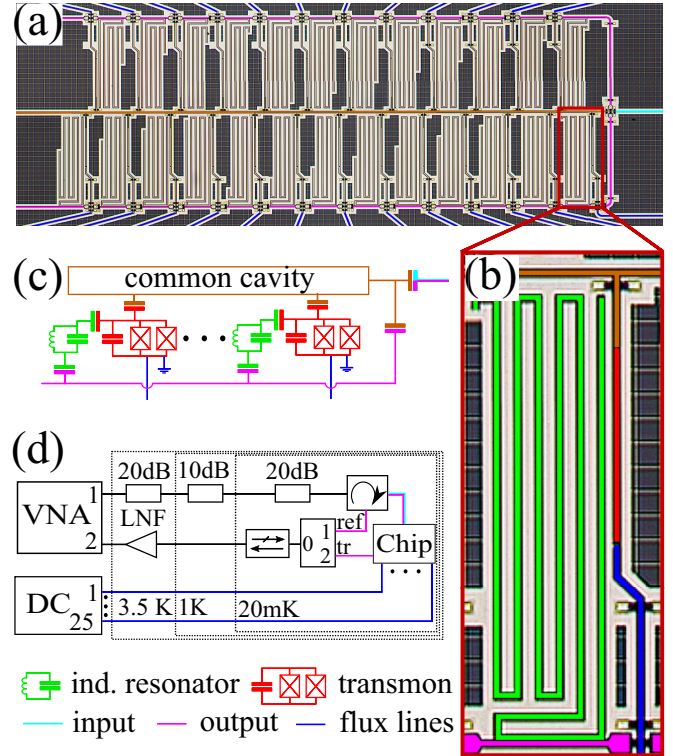


FIG. 1. Superconducting circuit and scheme of measurement. (a) False-colored optical photograph of the quantum metamaterial implemented as a chip with 25 superconducting qubits (transmons). (b) Enlarged fragment of the setup showing a single qubit, its individual readout resonator, flux bias line, and a fragment of the common cavity. (c) Equivalent electric circuit of the device. (d) Setting of the microwave measurement.

bias line (blue color) that allows one to tune the excitation frequency of a particular qubit. There are 25 individual control lines in total; they are implemented as asymmetric SQUIDs connected to a multichannel dc source. Fabrication steps of the device are described in Appendix B. Each of the qubits is capacitively coupled to an individual readout resonator [panel (b), green color]. These resonators have different lengths and frequencies and operate in a dispersive regime. This allows us to address each of the qubits individually through this feed line using frequency multiplexing, perform two-tone spectroscopy of qubits, and perform calibration of the frequency controls (Appendix C).

The common cavity is connected to its own microwave feedline in a butt-port geometry. Readout resonators are notch-port coupled to a common cavity and are connected to the output line [magenta color in the circuit shown in panel (d)].

We perform measurements of the reflection and transmission amplitudes,  $S_{11}$  and  $S_{21}$ , with the use of a microwave circulator and a switch. In  $S_{11}$  measurements, the incident signal is sent to the common cavity and reflected back. In  $S_{21}$  measurements, the incident signal excites qubit modes and leaves the chip through the individual resonators coupled to qubits.

The measurement scheme is shown in Fig. 1(c). The microwave drive tone, sent from the vector network analyzer

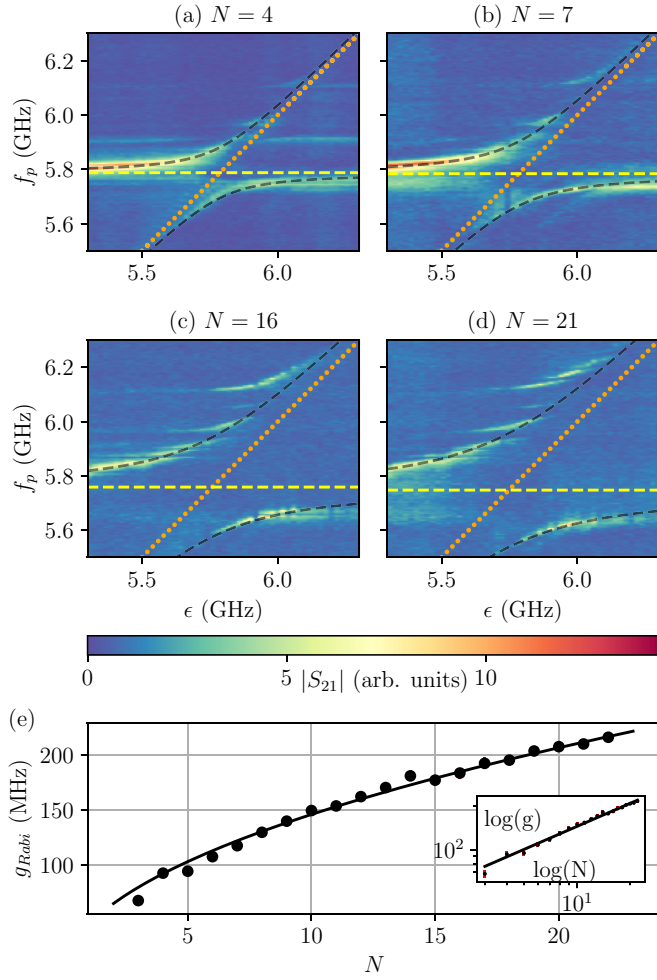


FIG. 2. Spectrum of collective bright (Rabi) modes. (a)–(d) Reflection amplitude  $|S_{21}|$  measured for different numbers of tunable qubits ( $N = 4, 7, 16, 21$ ). Black dashed curves are  $\nu_{\pm}$  energies of Rabi satellites predicted by the Tavis-Cummings model. Yellow dashed lines stand for the bare cavity mode frequency  $\nu_c$ . Orange dotted lines are bare frequencies of tunable qubits. (e)  $N^{1/2}$  scaling of Rabi splittings  $g_{\text{Rabi}}$  for  $N = 3, \dots, 23$  qubits tuned into the resonance with the cavity. Inset: the data in logarithmic coordinates fitted by  $g_{\text{Rabi}} = gN^\alpha$  (solid line).

(VNA), is attenuated by 50 dB before entering the chip. After passing through the chip, the signal is amplified and measured by the VNA, yielding the complex transmission amplitude  $S_{21}$ . Due to long attenuation and amplification chains,  $S_{21}$  is not calibrated. Thus the data are presented relative to an arbitrary level hereafter.

The spectroscopy data for  $S_{21}$ , where frequencies of resonant qubits,  $\epsilon = \epsilon_j$ , and probe signal  $f_p$  vary, are shown in Figs. 2(a)–2(d). Here we present results for  $N = 4, 7, 16$ , and 21 resonant qubits. These measurements are performed using the specific calibration procedure (Appendix C). Bright anti-crossings marked by black dashed curves are the energies of Rabi collective modes  $\nu_{\pm}$ . Yellow dashed and red dotted lines are bare frequencies of the cavity and resonant qubits. The increase of the gap with  $N$  indicates a bright-state coherence between the qubit array and photon mode.

#### IV. VACUUM RABI SPLITTING

The first important result of this work is the demonstration of  $N^{1/2}$  scaling in the Rabi splitting,  $g_{\text{Rabi}}$ , as a function of  $N$ , which is the number of qubits tuned into the resonance with the cavity. In Fig. 2(d) the dependence of  $g_{\text{Rabi}}(N)$ , where  $N$  changes from 3 to 23, is demonstrated. The theoretical dependence  $g_{\text{Rabi}} = g\sqrt{N}$  (solid curve) shows good agreement with the experimental data (dots). In the inset these data are shown in logarithmic coordinates. The points are approximated by  $g_{\text{Rabi}} = gN^\alpha$  with two fitting parameters,  $g$  and  $\alpha$ . The exponent is found as  $\alpha = 0.528 \pm 0.013$  and the qubit-cavity coupling as  $g = 42 \pm 3$  MHz. We note that previously, to our knowledge, the  $N^{1/2}$  scaling in the Rabi splitting between two bright states has been observed with ensembles of up to six tunable qubits [37]. Here, in spite of rising complexity of the measurement setup, we were able to bring into the collective bright states an ensemble of almost 4 times larger number of tunable qubits. It should be mentioned that  $N^{1/2}$  scaling is robust against errors in the resonance condition,  $\nu_c = \epsilon$ . The error results in a small ( $\sim 1/N$ ) relative deviation of  $g_{\text{Rabi}}$  from the power law. The estimation follows from the expressions for frequencies of bright modes  $\nu_{\pm}$ .

#### V. TRANSMISSION IN A DISORDERED METAMATERIAL

The most relevant result of this work is measurements of  $S_{21}$  in a mesoscopic metamaterial with large but finite number of qubits  $N$  and tunable disorder in their fundamental transition frequencies. Here, fluctuations are induced by the diagonal disorder in  $\epsilon_j$ . The disorder results in coupling of the pure dark states (with energies close to  $\nu_c$ ) to the cavity mode. The partial brightening shifts randomly the amplitude and phase of  $S_{21}$ .

Before we analyze fluctuations, we present transmission spectra in the disordered metamaterial. They are shown in Fig. 3. In these measurements we used up to 17 qubits which are chosen such that their individual resonators have frequencies not very close to  $\nu_c = 5.755$  GHz, while the rest of the qubits were detuned down to 5 GHz and play no role. As a result, we suppress a coupling to individual resonators in the spectral range of 5.65–5.95 GHz. The disorder is introduced artificially by applying random frequency shifts to all qubits with frequency spreads of  $\Delta = 20, 30, 50, 60, 70, 80$ , and 120 MHz. Transmission data for each probe frequency were averaged over 40 s to reduce the noise level. There are peaks at various frequencies in spectra for different disorder realizations. According to the above, we are rather certain that we detected dark states manifested by these peaks and not frequency shifts of individual resonators due to their coupling to the common cavity. Additional measurements that proof that we detected dark states were also carried out (Appendix D).

Panels (a)–(g) in Fig. 3 correspond to a particular spread of qubit frequencies  $\Delta$ . There are three curves in each panel, corresponding to three particular realizations of disordered  $\{\epsilon_j\}_{j=1}^N$  (black lines indicate qubit frequencies in each curve). Frequencies  $\{\epsilon_j\}_{j=1}^N$  are chosen such that they have a particular spread, i.e.,  $\langle \epsilon_j^2 \rangle - \langle \epsilon_j \rangle^2 = \Delta^2$ . The orange dashed line corresponds to the resonator frequency  $\nu_c$ . The large side

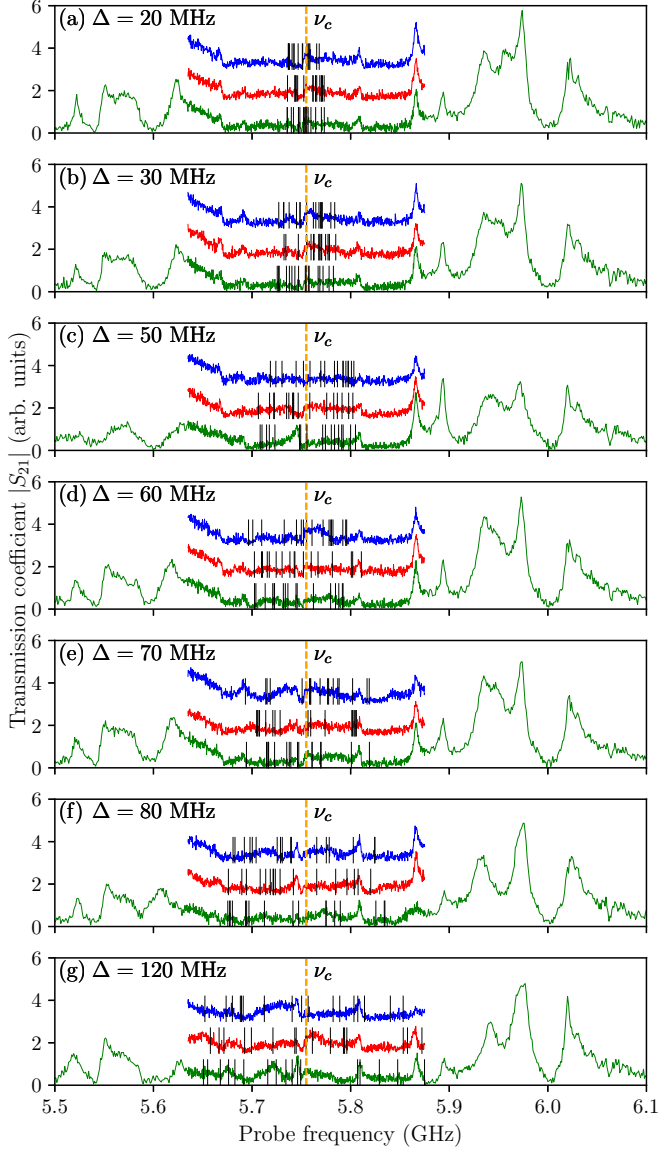


FIG. 3. Microwave spectroscopy of disordered metamaterial with 17 qubits. The data for transmission coefficient  $|S_{21}|$  is presented. Average qubit frequency is tuned into the resonance with the cavity,  $\langle \epsilon \rangle = \nu_c$ . Panels (a)–(g) correspond to different spreads  $\Delta$  in qubit frequencies. Different realizations of random frequency offsets are shown in different colors and location [green (lower), blue (upper), and red (middle)]. Black solid lines denote bare qubit frequencies. Orange dashed lines show the common resonator frequency.

peaks on the green curves are due to individual qubit readout resonators.

## VI. MESOSCOPIC FLUCTUATIONS

Let us address the average values of  $|\langle S_{21} \rangle|$  and  $\langle |\Delta S_{21}|^2 \rangle$  in the presence of disorder. Hereafter, the probe signal is tuned to the cavity mode frequency,  $f_p = \nu_c = \langle \epsilon \rangle$ ; hence, Eqs. (3) and (4) are applicable. The measurement results for  $|\langle S_{21} \rangle|$  and  $\langle |\Delta S_{21}|^2 \rangle$  are shown in Figs. 4(a) and 4(b), respectively. All points are obtained from averaging over 1000 disorder

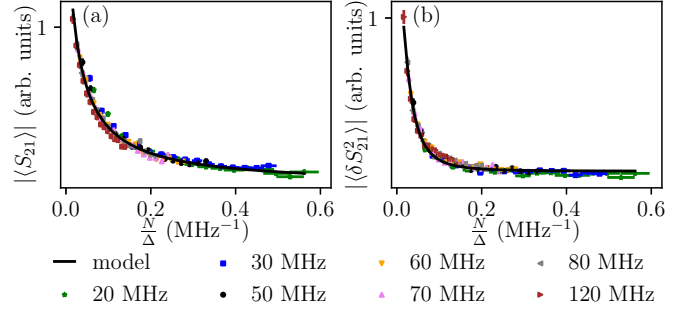


FIG. 4. Results for transmission coefficient and its fluctuations averaged by different disorder realizations. Different colors and markers stand for different spreads (see bottom of the figure). (a) Averaged transmission amplitude  $|\langle S_{21} \rangle|$ . (b) Averaged mesoscopic fluctuations  $\langle |\Delta S_{21}|^2 \rangle$ . Black lines are fitting theoretical curves given by Eq. (3) in (a) and by Eq. (4) in (b).

realizations. Different colors correspond to different values of  $\Delta$ . Here we present the data for  $|\langle S_{21} \rangle|$  and  $\langle |\Delta S_{21}|^2 \rangle$  as a function of  $N/\Delta$  for all spreads and  $N$ . The experimental data is fitted by the formulas  $|\langle S_{21} \rangle| = \left| \frac{a}{(\kappa + \pi g^2 N / \Delta)^\gamma} + c_1 \right|$  and  $\langle |\Delta S_{21}|^2 \rangle = \frac{b(N/\Delta)^\beta}{(\kappa + \pi g^2 N / \Delta)^\delta} + c_2$ , where the exponents are found as  $\gamma = 1.001 \pm 0.005$ ,  $\beta = 1.01 \pm 0.02$ , and  $\delta = 4 \pm 0.008$ . Their values show good agreement with theoretical predictions. Parameters  $c_1$  and  $c_2$  are phenomenological corrections that take into account shunting of the circuit probe signal due to interference between the cavity and background transmission (Fano resonance), and thermal noise, which we could not avoid in our measurements. The values of  $\beta$ ,  $\gamma$ , and  $\delta$  are obtained by least-squares fitting of the measurements. We account for the finite values of  $c_1$  and  $c_2$  using the data-processing procedure described in Appendix E. After subtraction of the background scattering ( $c_1$  and  $c_2$  parameters) we obtain good agreement between the processed data and predicted analytical dependence (black line in Fig. 4).

Equations (3) and (4) provide a characteristic number of resonant qubits  $N_0 \sim \frac{\Delta}{2\pi\Gamma}$ , above which a crossover from mesoscopic behavior to that of a thermodynamic limit occurs. The estimation follows from the matching condition  $\langle |\Delta S_{21}|^2 \rangle \sim \langle S_{21} \rangle^2$ , where we assume  $\kappa$  is smaller than  $g^2 \frac{N}{\Delta}$ . (For our setup,  $\kappa \approx 30$  MHz and  $\Gamma \approx 1$  MHz.) For instance, the measurements with minimal spread  $\Delta = 20$  MHz provide the estimated value of  $N_0 \sim 3$ –4. The data in Fig. 4 with such  $N$  and  $\Delta$  have a ratio  $\frac{N}{\Delta} > \frac{1}{2\pi\Gamma}$ , where  $\frac{1}{2\pi\Gamma} \approx 0.16$  MHz $^{-1}$ , corresponding to values of  $N$  that approach the thermodynamic limit formulated above.

## VII. CONCLUSION

We have studied experimentally an array of 25 tunable transmon qubits coupled to a common resonator. The tunability of qubits allowed us to simulate a diagonal disorder with preassigned distributions. First we have probed the collective modes of the qubit array by measuring the transmission amplitude of an external microwave signal. By tuning qubits one by one to the resonator frequency, we have observed the  $N^{1/2}$ -scaling law for the Rabi splitting as predicted by the Tavis-Cummings model. Our most interesting result is

measurements of the microwave transmission through the qubit metamaterial in the presence of synthesised disorder in qubit frequencies. We observed mesoscopic fluctuations emerging due to dark states which are very sensitive to disorder in qubit frequencies and their number in the ensemble. We observed a decay of the average value and fluctuations of transmission amplitude with increasing qubit number  $N$  and decreasing amplitude of the disorder. Thus, in the presence of disorder, adding more and more qubits promotes the collective bright state. The power-law decay in the transmission can evidence the semilocalized nature of disordered dark states [32], which can be a subject of further investigations. Our technique thus provides an on-chip quantum simulator of a crossover between the mesoscopic regime and the thermodynamic limit of the Tavis-Cummings model.

### ACKNOWLEDGMENTS

The experimental part of this work was performed with financial support from the Russian Science Foundation, Project No. 21-72-30026. D.S.S. and S.V.R. acknowledge the financial support of the theoretical part of the work by the Russian Foundation for Basic Research (RFBR) according to research Project No. 20-37-70028. D.S.S. acknowledges the support by RFBR research Project No. 20-52-12034, and by DFG Grant No. MI 658/13-1 within a joint DFG-RSF project.

## APPENDIX A: AVERAGING OF THE TRANSMISSION COEFFICIENT $S_{21}$

### 1. Definitions and assumptions

In this part we study fluctuations of the transmission coefficient  $S_{21}(\omega)$  acquired by the probe signal at frequency  $\omega$ . The transmission coefficient is a complex-valued function related to the photon-mode Green function  $\mathbf{G}_{\text{ph}}(\omega)$  as

$$S_{21}(\omega) = \sqrt{\gamma_{\text{in}}\gamma_{\text{out}}}\mathbf{G}_{\text{ph}}(\omega). \quad (\text{A1})$$

Here, loss rates  $\gamma_{\text{in}}$  and  $\gamma_{\text{out}}$  determine radiation from the resonator into the *in* and *out* waveguides, respectively. Our goal is to calculate fluctuations of  $S_{21}(\omega)$  averaged by different disorder realizations in qubit excitation frequencies.

Our calculations are based on following assumptions:

(1) The probe signal is small such the average photon number in the resonator is much smaller than 1. This assumption allows us to reduce the Hilbert space to that of a single excitation (either one photon or one qubit is excited). Also, this allows us to use the Tavis-Cummings model in a rotating-wave approximation.

(2) In analytical calculations we assume that the probe frequency  $\omega$  is tuned into a resonance with bare frequency of the resonator mode, i.e.,  $\omega = \nu_c$ . This allows us to find compact expressions.

(3) We assume the resonant condition between the resonator mode and all qubits on average as  $\nu_c = \langle \epsilon_j \rangle$ .

(4) We assume that disorder distribution functions are identical for all of the qubits. We suppose that their dispersions  $\Delta_j = \sqrt{\langle \epsilon_j^2 \rangle - \langle \epsilon_j \rangle^2}$  are identical, i.e.,  $\Delta_j = \Delta$ .

(5) The disorder parameter  $\Delta$  is supposed to be known. Also, we know the resonator loss rate,  $\kappa$ , the qubit loss rates

$\Gamma_j = \Gamma$ , and identical coupling constants  $g_j = g$  between the  $j$ th qubit and the resonator.

(6) The distribution probability  $p(\delta\epsilon_j)$  for random qubit detunings  $\delta\epsilon_j = \epsilon_j - \langle \epsilon_j \rangle$  is flat:

$$p(\delta\epsilon_j) = \frac{1}{\Delta}\theta(\Delta/2 - |\delta\epsilon_j|). \quad (\text{A2})$$

Here  $\delta\epsilon_j \in [-\Delta/2; \Delta/2]$  and  $p(\delta\epsilon_j)$  is normalized to unity.

### 2. Calculation of the photon Green function

The Tavis-Cummings model (for a particular realization of qubit frequencies  $\epsilon_j$  and different couplings  $g_j$ ) reads as

$$\hat{H} = \nu_c \hat{a}^\dagger \hat{a} + \sum_{j=1}^N \epsilon_j \hat{\sigma}_j^+ \hat{\sigma}_j^- + \sum_{j=1}^N g_j (\hat{\sigma}_j^+ \hat{a} + \hat{a}^\dagger \hat{\sigma}_j^-). \quad (\text{A3})$$

Here,  $\hat{a}^\dagger$  and  $\hat{a}$  are the photon creation and annihilation operators, and  $\hat{\sigma}_j^+$  and  $\hat{\sigma}_j^-$  are raising and lowering operators acting upon  $j$ th qubit. This Hamiltonian can be represented as an  $N+1$ -dimensional matrix  $\mathcal{H}_{i,j} = \langle \psi_i | \hat{H} | \psi_j \rangle$  after the projection of  $\hat{H}$  on a single excitation basis,  $\{|\psi_i\rangle\}_{i=1}^{N+1} = \{\hat{a}^\dagger |g.s.\rangle; \hat{\sigma}_1^+ |g.s.\rangle; \dots; \hat{\sigma}_N^+ |g.s.\rangle\}$ :

$$\mathcal{H} = \begin{bmatrix} \nu_c & \mathbf{g}^T \\ \mathbf{g} & h_{\text{q}} \end{bmatrix}. \quad (\text{A4})$$

Here we introduced the  $N$ -dimensional vector  $\mathbf{g} = (g_1; g_2; \dots; g_N)^T$  and the diagonal matrix for the qubit ensemble  $h_{\text{q},i,j} = \delta_{i,j}\epsilon_j$ . The respective Green function is

$$\mathcal{G}(\omega) = \begin{bmatrix} G_{\text{ph}}^{-1}(\omega) & -\mathbf{g}^T \\ -\mathbf{g} & \mathbf{G}_{\text{q}}^{-1}(\omega) \end{bmatrix}^{-1}. \quad (\text{A5})$$

It takes into account loss rates, which can be written through the bare Green functions of the lumped resonator and qubit modes,  $G_{\text{ph}}$  and  $G_{\text{q}}$ , respectively. They read as follows: The resonator Green function is

$$G_{\text{ph}}(\omega) = \frac{1}{\omega + i\kappa - \nu_c}. \quad (\text{A6})$$

Qubit modes are encoded by the diagonal matrix  $G_{\text{q}}$ , and its elements are  $G_{\text{q},i,j} = \delta_{i,j}G_{\text{q},j}$ . They read

$$G_{\text{q},j}(\omega) = \frac{1}{\omega + i\Gamma - \epsilon_j}, \quad j \in [1, N]. \quad (\text{A7})$$

The inverse matrix  $\mathcal{G}^{-1}$  (A5) has nonzero elements on the diagonal and on the upper row and left column determined by  $\mathbf{g}^T$  and  $\mathbf{g}$ , while other elements are equal to zero. The first diagonal element of  $[\mathcal{G}(\omega)]_{1,1}$  corresponds to the photon Green function in the hybrid system, written  $\mathcal{G}_{\text{ph}}(\omega)$ . It is found after an expansion by the nondiagonal  $\mathbf{g}^T$  and  $\mathbf{g}$  in (A5) and following resummation of even-order terms. The result is

$$\mathcal{G}_{\text{ph}}(\omega) = \frac{1}{G_{\text{ph}}^{-1}(\omega) - \mathbf{g}^T \mathbf{G}_{\text{q}}(\omega) \mathbf{g}}. \quad (\text{A8})$$

It takes into account disorders in qubit frequencies and in couplings through the product in the denominator:

$$\mathbf{g}^T \mathbf{G}_{\text{q}}(\omega) \mathbf{g} = \sum_{j=1}^N g_j^2 G_{\text{q},j}(\omega). \quad (\text{A9})$$

### 3. Finite-size fluctuations of $S_{21}$

We consider complex-valued  $S_{21}$  from (A1) at zero detuning (i.e., we probe a response at the bare resonator frequency  $\nu_c$ ). It is related to the Green function  $\mathcal{G}_{\text{ph}}(\omega_r)$  and reads

$$S_{21}(\omega = \nu_c) = \sqrt{\gamma_{\text{in}}\gamma_{\text{out}}} \left[ g^2 \sum_{j=1}^N \frac{\delta\epsilon_j}{(\delta\epsilon_j)^2 + \Gamma^2} + i \left( \kappa + g^2 \Gamma \sum_{j=1}^N \frac{1}{(\delta\epsilon_j)^2 + \Gamma^2} \right) \right]^{-1}. \quad (\text{A10})$$

Let us analyze the disorder effects starting from a formal limit of infinitely large  $N$ . Then the mesoscopic corrections due to  $1/N$  with finite  $N$  are to be calculated.

There is a self-averaging in the limit of large enough  $N$ , namely, the sums in (A10) are treated as integrals over continuous-variable  $\epsilon \in [-\frac{\Delta}{2}; \frac{\Delta}{2}]$  with  $p(\epsilon)$  from (A2). This gives

$$\sum_{j=1}^N \frac{\delta\epsilon_j}{(\delta\epsilon_j)^2 + \Gamma^2} = N \int p(\epsilon) \frac{\epsilon d\epsilon}{\epsilon^2 + \Gamma^2} = 0, \quad (\text{A11})$$

$$\sum_{j=1}^N \frac{1}{(\delta\epsilon_j)^2 + \Gamma^2} = N \int p(\epsilon) \frac{d\epsilon}{\epsilon^2 + \Gamma^2} = \frac{\pi N}{\Delta\Gamma}. \quad (\text{A12})$$

(Here we assumed  $\Delta \gg \Gamma$  and calculated the integrals in infinite limits.) Thus, after these integrations we find the averaged  $\langle S_{21} \rangle$ :

$$\langle S_{21} \rangle = \sqrt{\gamma_{\text{in}}\gamma_{\text{out}}} \frac{-i}{\kappa + \pi g^2 N / \Delta}. \quad (\text{A13})$$

Now we address the mesoscopic correction to this result due to random variables given by the first sum,  $g^2 \sum_{j=1}^N \frac{\delta\epsilon_j}{(\delta\epsilon_j)^2 + \Gamma^2}$ , in the square brackets of (A10). We expand  $S_{21}$  by the first order in this random-valued sum:

$$S_{21} \approx \frac{-i\sqrt{\gamma_{\text{in}}\gamma_{\text{out}}}}{\kappa + \pi g^2 N / \Delta} \left( 1 + \frac{ig^2}{\kappa + \pi g^2 N / \Delta} \sum_{j=1}^N \frac{\delta\epsilon_j}{(\delta\epsilon_j)^2 + \Gamma^2} \right). \quad (\text{A14})$$

According to Eqs. (A13) and (A14), we find the random deviation  $\delta S_{21}$  from the averaged value  $\langle S_{21} \rangle$  for a particular realization of values  $\epsilon_j$  (we still work with the complex-valued quantity):

$$\delta S_{21} = S_{21} - \langle S_{21} \rangle = e^{i\varphi_0} \frac{g^2 \sqrt{\gamma_{\text{in}}\gamma_{\text{out}}}}{(\kappa + \pi g^2 N / \Delta)^2} \sum_{j=1}^N \frac{\delta\epsilon_j}{(\delta\epsilon_j)^2 + \Gamma^2}. \quad (\text{A15})$$

At this step we find its absolute squared and averaged value:

$$\langle |\delta S_{21}|^2 \rangle = \frac{g^4 \gamma_{\text{in}} \gamma_{\text{out}}}{(\kappa + \pi g^2 N / \Delta)^4} \times \sum_{i,j=1}^N \left\langle \frac{\delta\epsilon_i \delta\epsilon_j}{((\delta\epsilon_i)^2 + \Gamma^2)((\delta\epsilon_j)^2 + \Gamma^2)} \right\rangle. \quad (\text{A16})$$

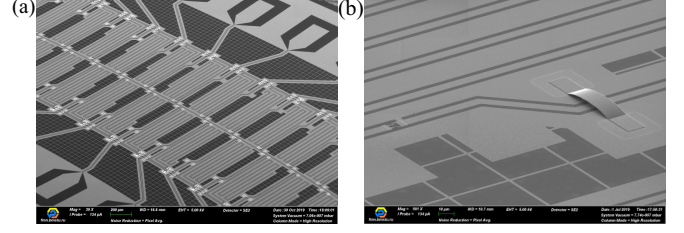


FIG. 5. (a) SEM image of a 25-qubit array. (b) SEM image of a Josephson junction SQUID with low-impedance crossover.

The cross terms with  $i \neq j$  in the average (A16) cancel out. Hence,

$$\begin{aligned} & \sum_{i,j=1}^N \left\langle \frac{\delta\epsilon_i \delta\epsilon_j}{((\delta\epsilon_i)^2 + \Gamma^2)((\delta\epsilon_j)^2 + \Gamma^2)} \right\rangle \\ &= \sum_{j=1}^N \left\langle \frac{\delta\epsilon_j^2}{((\delta\epsilon_j)^2 + \Gamma^2)^2} \right\rangle = N \int p(\epsilon) \frac{\epsilon^2 d\epsilon}{(\epsilon^2 + \Gamma^2)^2} \\ &= \frac{\pi N}{2\Gamma\Delta}. \end{aligned} \quad (\text{A17})$$

[We note that  $\langle |\delta S_{21}|^2 \rangle$  decays faster than  $\langle S_{21} \rangle$  at large  $N$ , which means the expansion in (A14) is a controllable approximation.] Finally, we find *relative* mesoscopic fluctuations of  $S_{21}$ , combining Eqs. (A13), (A16), and (A17), which reads

$$\frac{\sqrt{\langle |\delta S_{21}|^2 \rangle}}{|\langle S_{21} \rangle|} = \frac{g^2}{\kappa + \pi g^2 N / \Delta} \sqrt{\frac{\pi N}{2\Gamma\Delta}}. \quad (\text{A18})$$

We note that if one assumes that the resonator's relaxation is small,  $\kappa \ll g^2 N / \Delta$ , we find the following scaling where  $g$  does not appear:

$$\frac{\sqrt{\langle |\delta S_{21}|^2 \rangle}}{|\langle S_{21} \rangle|} = \sqrt{\frac{1}{N} \frac{\Delta}{2\pi\Gamma}}. \quad (\text{A19})$$

However, experimental observation of this scaling requires large  $N$  and small  $\kappa$ , which are not realized in our device.

## APPENDIX B: SAMPLE FABRICATION

To fabricate the superconducting chip based on the array of 25 transmon qubits coupled to a common coplanar resonator we use the three-stage process. The process includes following stages: (I) epitaxial Al base layer deposition using a two-step SCULL process [38] and Al patterning with laser direct lithography (including transmon capacitor ground plane, waveguides, resonators, and flux bias lines); (II) double-angle evaporation of Josephson junctions followed by liftoff; (III) resist-based low-impedance crossover fabrication. Scanning electron microscopy (SEM) images of metamaterial and enlarged fragment of a Josephson junction SQUID are shown in Fig. 5.

The fabrication process starts with a multistep wet chemical cleaning of a high-resistivity intrinsic silicon sample ( $\rho > 10000 \Omega \text{ cm}$ ,  $525 \mu\text{m}$  thick) in a Piranha solution (1 : 4) followed by native oxide removal in HF (1 : 50) for 120 s. Immediately after a 100-nm-thick epitaxial Al base layer

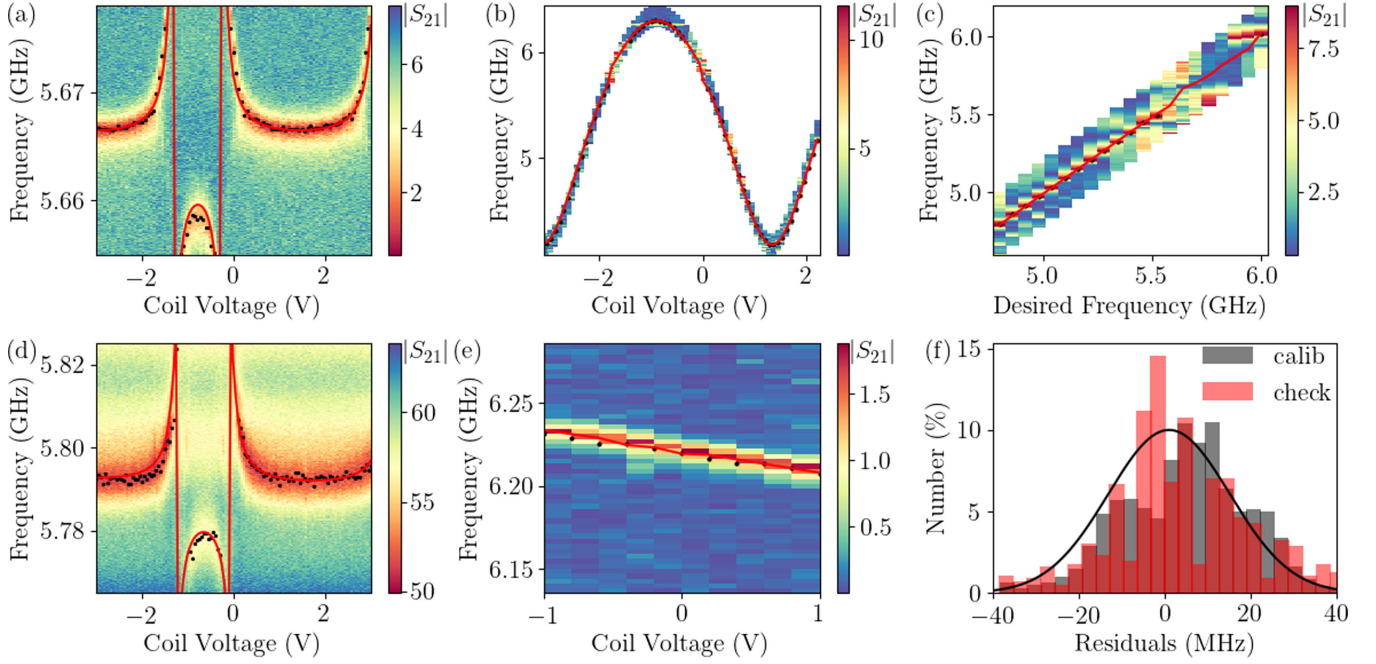


FIG. 6. Typical spectra used for calibration and fitting residuals. Response amplitudes ( $|S_{21}|$ ) are given in arbitrary units. (a) Single-tone spectroscopy of individual resonator. (b) Adaptive two-tone spectroscopy. (c) Check accuracy of setting qubits into desired frequency. (d) Single-tone spectroscopy of common cavity. (e) Two-tone spectroscopy tuning voltage of coil connected to another qubit. (f) Distributions of residuals from two-tone spectra used for calibration or check frequencies. Solid black line was calculated from dispersion and average of distribution. (a)–(e) Red solid lines were calculated using Tavis-Cummings model, black dots is data used for fitting task.

is deposited with a UHV e-beam evaporation SCULL technique [38] followed by its direct laser lithography patterning and dry etching in  $\text{BCl}_3/\text{Cl}_2$ -based gasses. Then a two-layer e-beam resist stack (300-nm-thick PMMA e-beam resist on top of a 500-nm-thick MMA copolymer) is spin coated followed by 50-kV e-beam exposure. After development and oxygen plasma treatment, we performed UHV e-beam shadow evaporation of Al-AlOx-Al Josephson junctions ( $62^\circ/0^\circ$ , 25/45 nm). Low-impedance freestanding crossovers are fabricated by means of a four-step [39] process: (I) crossovers pads laser lithography, (II) 300-nm-thick Al film e-beam deposition, (III) crossover topology laser lithography, and (IV)  $\text{BCl}_3/\text{Cl}_2$ -based dry plasma etching. Finally, we stripped both resist layers in a N-Methyl-2-pyrrolidone solvent.

### APPENDIX C: CALIBRATION

Spectroscopic measurements were performed to determine device parameters such as Josephson energies of SQUID junctions, capacitive energies, coupling between qubits and common cavity, qubits and individual resonators, mutual inductance between coils and qubits, frequencies of resonators, and flux biases of the SQUIDs. Typical results of these measurements are presented in Figs. 6(a), 6(b), 6(d), and 6(e).

For each flux configuration, the frequency corresponding to a maximal two-tone response is taken as qubit frequency. Outlier points are dropped after we extract device parameters by fitting data with the Tavis-Cummings model (C1) extended with the individual resonators ( $v_j$ ). We also consider the dependence of the coupling coefficients to the common cavity

( $g_j = k_j \sqrt{\epsilon_j}$ ) and to individual readout resonators ( $g_j^{\text{ind}} = k_j^{\text{ind}} \sqrt{\epsilon_j}$ ) on qubit frequencies ( $\epsilon_j$ ):

$$\begin{aligned} \hat{H} = & \sum_{j=1}^N v_j \hat{a}_j^\dagger \hat{a}_j + \sum_{j=1}^N \epsilon_j \hat{\sigma}_j^+ \hat{\sigma}_j^- + v_c \hat{a}^\dagger \hat{a} \\ & + \sum_{j=1}^N k_j^{\text{ind}} \sqrt{\epsilon_j} (\hat{a}_j^\dagger + \hat{a}_j) (\hat{\sigma}_j^+ + \hat{\sigma}_j^-) \\ & + \sum_{j=1}^N k_j \sqrt{\epsilon_j} (\hat{a}^\dagger + \hat{a}) (\hat{\sigma}_j^+ + \hat{\sigma}_j^-). \end{aligned} \quad (\text{C1})$$

For the dependence of bare transmon frequency on the SQUID flux we use the following formula:

$$\begin{aligned} \epsilon(\phi) = & \sqrt{8E_C} ((E_{J1} + E_{J2})^2 \cos^2 \phi \\ & + (E_{J1} - E_{J2})^2 \sin^2 \phi)^{\frac{1}{4}} - E_C, \end{aligned} \quad (\text{C2})$$

where  $E_{J1}$  and  $E_{J2}$  are Josephson energies of the dc SQUID junctions,  $E_C$  is the transmon charging energy, and  $\phi = 2\pi \frac{\Phi}{\Phi_0}$  is the dimensionless magnetic flux threaded by the SQUID. We assume the linear dependence of SQUID fluxes on the dc voltage is applied to the coils,

$$\phi_i = \sum L_{ij} V_j + \phi_i^0, \quad (\text{C3})$$

where index  $i$  corresponds to the qubit number,  $j$  to the coil number, and  $\phi^0$  is the frozen dimensionless magnetic flux in the SQUID. The effective eigenmode of a specific transmon was chosen as the frequency of the mode with the largest participation in this transmon. The fitting was performed with a



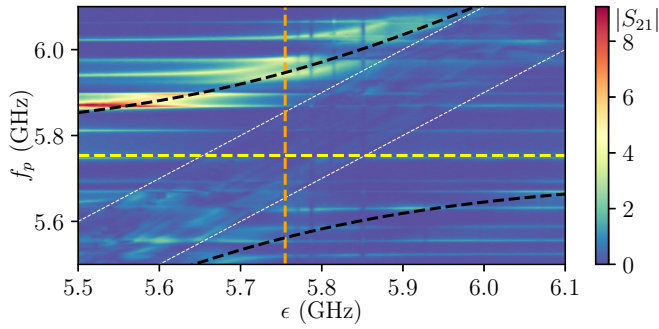


FIG. 7. Transmission spectrum for detection of dark states. Transmission amplitude  $|S_{21}|$  is given in arbitrary units. Yellow horizontal dashed line stands for bare cavity mode frequency  $\nu_c$ . Black dashed curves are bare frequencies of tunable qubits. Orange vertical dashed line corresponds to the measurements presented in Fig. 3, when the central frequency of the qubit ensemble is equal to the bare frequency of the common cavity. White dashed lines show the area of possible qubits frequencies.

least-squares cost function. The standard deviation is 20 MHz. The distribution of residuals is shown on Fig. 6(f) (black bar).

When setting a transmon to some frequency, we do not set the bare frequency of the transmon but the eigenfrequency of the transmon-individual resonator system. The bare qubit frequency is calculated using a coupled linear oscillator model  $\epsilon_c = \frac{\epsilon + \nu}{2} \pm \frac{\sqrt{(\epsilon - \nu)^2 + 4k\epsilon}}{2}$ , where  $\epsilon_c$  corresponds to the eigenfrequency of the coupled system. After that, fluxes are calculated from Eq. (C2), and then the linear system of equations (C3) is solved.

To evaluate frequency control accuracy independently, we performed a two-tone spectroscopy measurement, setting all qubits to equal desired frequency and then tuning one of them in some range, while others remain in their original position. A typical result of these measurements and the distribution of residuals are shown in Figs. 6(c) and 6(f), correspondingly. The standard deviation is also equal to 20 MHz. We consider this value as the frequency control error.

#### APPENDIX D: DETECTION OF DARK STATES

We carried out measurements to ensure that dark states are observable in our experiments. We tuned the central frequency of the ensemble of qubits with fixed disorder and provide transmission measurements. The results of these measurements are presented in Fig. 7. White dashed lines show the bounds for the qubit frequencies in the ensemble. Several continuous lines are visible inside white bounds that are parallel to the white lines. This fact reveals that the system response is changed with the central frequency of the qubit ensemble, i.e., each line corresponds to a certain dark state. This is an argument for successful detection of dark states for data presented in Fig. 3. Also, Fig. 7 shows that individual resonator frequencies within the range between 5.65 and 5.95 GHz do not depend on the central frequency of the qubit ensemble, as pointed out in the main text.

#### APPENDIX E: PROCESSING OF EXPERIMENTAL DATA

The variance in experimental data can be due to various reasons, such as, e.g., specific realizations of flat distribution, calibration of qubit frequencies, interference between the cavity and background transmission (Fano resonance), and thermal noise. The influence of some of these factors is discussed below.

Average transmission amplitudes for different spreads  $\Delta$  are shown in Fig. 8(a). From Eq. (A13) we expect a straight line dependence for real and imaginary parts of  $S_{21}$  with increasing number of qubits  $N$  for each value of  $\Delta$ . It is seen from Fig. 8(a) that experimental curves are close to straight lines but tend to the same nonzero value. As it is mentioned in the main text, one reason for such behavior is the appearance of Fano resonance. In our postprocessing we had to introduce phenomenological corrections to eliminate this parasitic effect. Corrections are selected the same for all curves. A typical example of such processing is shown in Fig. 8(b), where you can see the dependence of the absolute value of the transmission signal on the number of resonant qubits for the initial data and for the data after elimination of the Fano resonance influence.

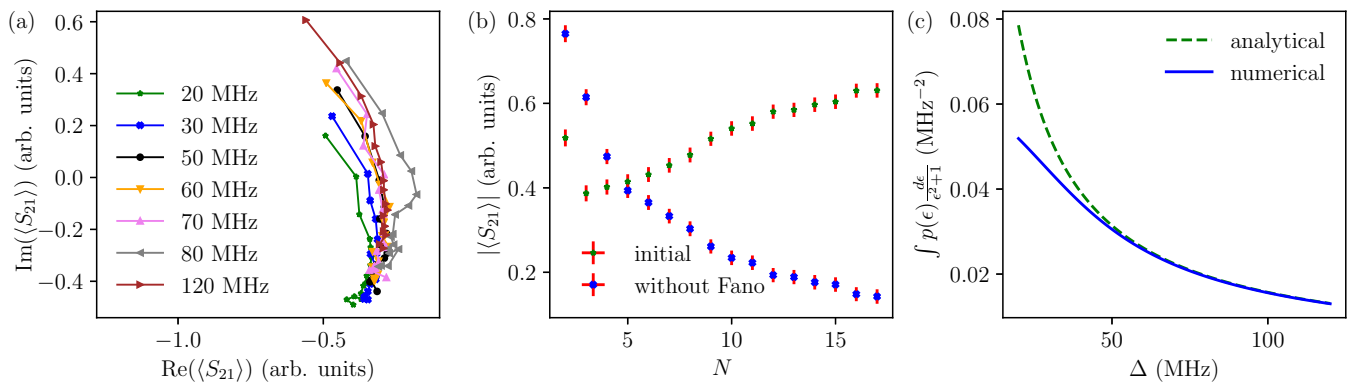


FIG. 8. Processing of experimental data. (a) Average of transmission amplitude on complex plane from the number of resonant qubits for different distribution spreads  $\Delta$ . (b) Dependence of the absolute value of average transmission amplitude on  $N$  for initial experimental data and after elimination of the Fano resonance. (c) The integral (A12) value dependence on the random distribution spread calculated analytically and numerically to account for calibration errors.

An additional processing step was made to take into account the difference between the real distribution and the random flat distribution due to calibration errors, Fig. 6(f). These errors prevent us from using a simple analytical calculation of the integral in Eq. (A12). The comparison of the analytical and numerical solution of this integral for different spreads  $\Delta$  is shown in Fig. 8(c). A significant discrepancy is observed at small values of  $\Delta$ . For subsequent calculations presented in the main text we used a numerical approach in order to determine the effective width of distribution.

The influence of these errors is shown in Fig. 9, where the presented inverted averaged transmission coefficient  $|1/\langle S_{21} \rangle|$  for the initial  $\Delta$  (a) and corrected (b). According to Eq. (A13), there should be a linear dependence between the inverted transmission  $|1/\langle S_{21} \rangle|$  and the ratio  $N/\Delta$ , up to a constant shift. The raw data is well fitted by different lines for each width of distribution, while for processed data it is only by one line.

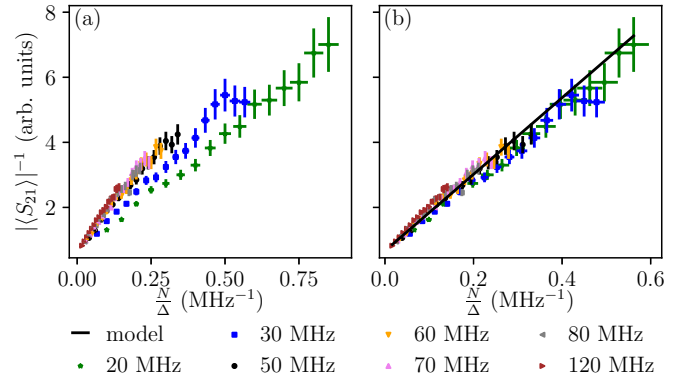


FIG. 9. Inverted transmission coefficient  $|1/\langle S_{21} \rangle|$  as a function of the ratio  $N/\Delta$ . Different colors and markers stand for different spreads (see bottom of the figure). (a) The raw data with initial  $\Delta$ . (b) Processed data with corrected  $\Delta$ . Black line in (b) is the fitting curve which is given by Eq. (A13).

- [1] F. Arute, K. Arya, R. Babbush, D. Bacon, J. C. Bardin, R. Barends, R. Biswas, S. Boixo, F. G. S. L. Brandao, D. A. Buell, B. Burkett, Y. Chen, Z. Chen, B. Chiaro, R. Collins, W. Courtney, A. Dunsworth, E. Farhi, B. Foxen, A. Fowler *et al.*, *Nature (London)* **574**, 505 (2019).
- [2] A. A. Clerk, K. W. Lehnert, P. Bertet, J. R. Petta, and Y. Nakamura, *Nat. Phys.* **16**, 257 (2020).
- [3] R. Barends, L. Lamata, J. Kelly, L. García-Álvarez, A. G. Fowler, A. Megrant, E. Jeffrey, T. C. White, D. Sank, J. Y. Mutus, B. Campbell, Y. Chen, Z. Chen, B. Chiaro, A. Dunsworth, I. C. Hoi, C. Neill, P. J. J. O'Malley, C. Quintana, P. Roushan *et al.*, *Nat. Commun.* **6**, 7654 (2015).
- [4] M. D. Schroer, M. H. Kolodrubetz, W. F. Kindel, M. Sandberg, J. Gao, M. R. Vissers, D. P. Pappas, A. Polkovnikov, and K. W. Lehnert, *Phys. Rev. Lett.* **113**, 050402 (2014).
- [5] Y. Chen, P. Roushan, D. Sank, C. Neill, E. Lucero, M. Mariantoni, R. Barends, B. Chiaro, J. Kelly, A. Megrant, J. Y. Mutus, P. J. J. O'Malley, A. Vainsencher, J. Wenner, T. C. White, Y. Yin, A. N. Cleland, and J. M. Martinis, *Nat. Commun.* **5**, 5184 (2014).
- [6] P. Roushan, C. Neill, Y. Chen, M. Kolodrubetz, C. Quintana, N. Leung, M. Fang, R. Barends, B. Campbell, Z. Chen, B. Chiaro, A. Dunsworth, E. Jeffrey, J. Kelly, A. Megrant, J. Mutus, P. J. J. O'Malley, D. Sank, A. Vainsencher, J. Wenner *et al.*, *Nature (London)* **515**, 241 (2014).
- [7] I. S. Besedin, M. A. Gorlach, N. N. Abramov, I. Tsitsilin, I. N. Moskalenko, A. A. Dobronosova, D. O. Moskalev, A. R. Matanin, N. S. Smirnov, I. A. Rodionov, A. N. Poddubny, and A. V. Ustinov, *Phys. Rev. B* **103**, 224520 (2021).
- [8] B. Murta, G. Catarina, and J. Fernández-Rossier, *Phys. Rev. A* **101**, 020302(R) (2020).
- [9] A. J. Hoffman, S. J. Srinivasan, S. Schmidt, L. Spietz, J. Aumentado, H. E. Türeci, and A. A. Houck, *Phys. Rev. Lett.* **107**, 053602 (2011).
- [10] C. Lang, D. Bozyigit, C. Eichler, L. Steffen, J. M. Fink, A. A. Abdumalikov, M. Baur, S. Filipp, M. P. da Silva, A. Blais, and A. Wallraff, *Phys. Rev. Lett.* **106**, 243601 (2011).
- [11] J. Goetz, S. Pogorzalek, F. Deppe, K. G. Fedorov, P. Eder, M. Fischer, F. Wulschner, E. Xie, A. Marx, and R. Gross, *Phys. Rev. Lett.* **118**, 103602 (2017).
- [12] A. Y. Dmitriev, R. Shaikhaidarov, T. Hönlgl-Decrinis, S. E. de Graaf, V. N. Antonov, and O. V. Astafiev, *Phys. Rev. A* **100**, 013808 (2019).
- [13] T. Hönlgl-Decrinis, R. Shaikhaidarov, S. E. de Graaf, V. N. Antonov, and O. V. Astafiev, *Phys. Rev. Appl.* **13**, 024066 (2020).
- [14] Y. Zhou, Z. Peng, Y. Horiuchi, O. V. Astafiev, and J. S. Tsai, *Phys. Rev. Appl.* **13**, 034007 (2020).
- [15] J. Braumüller, J. Cramer, S. Schlör, H. Rotzinger, L. Radtke, A. Lukashenko, P. Yang, S. T. Skacel, S. Probst, M. Marthaler, L. Guo, A. V. Ustinov, and M. Weides, *Phys. Rev. B* **91**, 054523 (2015).
- [16] P. Macha, G. Oelsner, J.-M. Reiner, M. Marthaler, S. André, G. Schön, U. Hübner, H.-G. Meyer, E. Il'ichev, and A. V. Ustinov, *Nat. Commun.* **5**, 5146 (2014).
- [17] A. Frisk Kockum, A. Miranowicz, S. De Liberato, S. Savasta, and F. Nori, *Nat. Rev. Phys.* **1**, 19 (2019).
- [18] P. Kirton, M. M. Roses, J. Keeling, and E. G. Dalla Torre, *Adv. Quantum Technol.* **2**, 1800043 (2019).
- [19] D. S. Shapiro, W. V. Pogosov, and Y. E. Lozovik, *Phys. Rev. A* **102**, 023703 (2020).
- [20] A. Biella, L. Mazza, I. Carusotto, D. Rossini, and R. Fazio, *Phys. Rev. A* **91**, 053815 (2015).
- [21] F. Vicentini, F. Minganti, R. Rota, G. Orso, and C. Ciuti, *Phys. Rev. A* **97**, 013853 (2018).
- [22] G. P. Fedorov, S. V. Remizov, D. S. Shapiro, W. V. Pogosov, E. Egorova, I. Tsitsilin, M. Andronik, A. A. Dobronosova, I. A. Rodionov, O. V. Astafiev, and A. V. Ustinov, *Phys. Rev. Lett.* **126**, 180503 (2021).
- [23] D. S. Shapiro, P. Macha, A. N. Rubtsov, and A. V. Ustinov, *Photonics* **2**, 449 (2015).
- [24] K. V. Shulga, P. Yang, G. P. Fedorov, M. V. Fistul, M. Weides, and A. V. Ustinov, *JETP Lett.* **105**, 47 (2017).

- [25] M. Tavis and F. W. Cummings, *Phys. Rev.* **170**, 379 (1968).
- [26] J. Koch, T. M. Yu, J. Gambetta, A. A. Houck, D. I. Schuster, J. Majer, A. Blais, M. H. Devoret, S. M. Girvin, and R. J. Schoelkopf, *Phys. Rev. A* **76**, 042319 (2007).
- [27] A. Smith, M. S. Kim, F. Pollmann, and J. Knolle, *npj Quantum Inf.* **5**, 106 (2019).
- [28] J. Braumüller, L. Ding, A. P. Vepsäläinen, Y. Sung, M. Kjaergaard, T. Menke, R. Winik, D. Kim, B. M. Niedzielski, A. Melville, J. L. Yoder, C. F. Hirjibehedin, T. P. Orlando, S. Gustavsson, and W. D. Oliver, *Phys. Rev. Appl.* **13**, 054079 (2020).
- [29] F. Arute, K. Arya, R. Babbush, D. Bacon, J. C. Bardin, R. Barends, A. Bengtsson, S. Boixo, M. Broughton, B. B. Buckley, D. A. Buell, B. Burkett, N. Bushnell, Y. Chen, Z. Chen, Y.-A. Chen, B. Chiaro, R. Collins, S. J. Cotton, W. Courtney *et al.*, [arXiv:2010.07965](https://arxiv.org/abs/2010.07965).
- [30] J. Feist and F. J. Garcia-Vidal, *Phys. Rev. Lett.* **114**, 196402 (2015).
- [31] J. Schachenmayer, C. Genes, E. Tignone, and G. Pupillo, *Phys. Rev. Lett.* **114**, 196403 (2015).
- [32] T. Botzung, D. Hagenmüller, S. Schütz, J. Dubail, G. Pupillo, and J. Schachenmayer, *Phys. Rev. B* **102**, 144202 (2020).
- [33] C. Berke, E. Varvelis, S. Trebst, A. Altland, and D. P. DiVincenzo, [arXiv:2012.05923](https://arxiv.org/abs/2012.05923).
- [34] V. V. Temnov and U. Woggon, *Phys. Rev. Lett.* **95**, 243602 (2005).
- [35] I. Diniz, S. Portolan, R. Ferreira, J. M. Gérard, P. Bertet, and A. Auffèves, *Phys. Rev. A* **84**, 063810 (2011).
- [36] G. S. Agarwal, *Phys. Rev. Lett.* **53**, 1732 (1984).
- [37] P. Yang, J. D. Brehm, J. Leppäkangas, L. Guo, M. Marthaler, I. Boverter, A. Stehli, T. Wolz, A. V. Ustinov, and M. Weides, *Phys. Rev. Appl.* **14**, 024025 (2020).
- [38] I. A. Rodionov, A. S. Baburin, A. R. Gabidullin, S. S. Maklakov, S. Peters, I. A. Ryzhikov, and A. V. Andriyash, *Sci. Rep.* **9**, 12232 (2019).
- [39] Z. Chen, A. Megrant, J. Kelly, R. Barends, J. Bochmann, Y. Chen, B. Chiaro, A. Dunsworth, E. Jeffrey, J. Y. Mutus, P. J. J. O'Malley, C. Neill, P. Roushan, D. Sank, A. Vainsencher, J. Wenner, T. C. White, A. N. Cleland, and J. M. Martinis, *Appl. Phys. Lett.* **104**, 052602 (2014).